Electric Single-Molecule Hybridization Detector for Short DNA Fragments

A. Y. Y. Loh,[†] C. H. Burgess,[‡] D. A. Tanase,[†] G. Ferrari,[§] M. A. McLachlan,[‡] A. E. G. Cass,[†] and T. Albrecht*[,†,∥]

[†]Department of Chemistry, Imperial College London, Exhibition Road, London SW7 2AZ, United Kingdom

[‡]Department of Materials and Centre for Plastic Electronics, Imperial College London, London SW7 2AZ, United Kingdom

[§]Dipartimento di Elettronica, Informazione e Bioingegneria, Politecnico di Milano, Piazza Leonardo da Vinci 32, Milano 20133, Italy

[∥]School of Chemistry, University of Birmingham, Edgbaston Campus, Birmingham B15 2TT, United Kingdom

ABSTRACT: By combining DNA nanotechnology and high-bandwidth single-molecule detection innanopipets, we demonstrate an electric, label-free hybridization sensor for short DNA sequences (<100 nucleotides). Such short fragments are known to occur as circulating cell-free DNA in various bodily fluids, such as blood plasma and saliva, and have been identified as disease markers for cancer and infectious diseases. To this end, we use as a model system an 88-mer target from the *RV1910c* gene in *Mycobacterium tuberculosis*, which is associated with antibiotic (isoniazid) resistance in TB. Upon binding to short probes attached to long carrier DNA, we show that resistive-pulse sensing in nanopipets is capable of identifying rather subtle structural differences, such as the hybridization state of the probes, in a statistically robust manner. With significant potential toward multiplexing and high-throughput analysis, our study points toward a new, single-molecule DNA-assay technology that is fast, easy to use, and compatible with point-of-care environments.

Nanopore devices are a new class of stochastic single-molecule sensors. As nanoscale analogues of the well-known Coulter counter, which is routinely used for cell counting in hospital environments, they have been developed for fast and label-free DNA sequencing.[1] This feat has now largely been achieved with (modified) biological pores, such as α-hemolysin.[2] However, resistive-pulse sensing with solid-state nanopores and nanopipets offers a range of other potential applications. These nanodevices are relatively easy to fabricate (especially nanopipets[3,4]) and there is usually considerable flexibility in their design with regards to the pore dimensions (diameter, channel length, and shape). This means that they can more readily be adapted to larger or more structurally complex analytes, including double-stranded (ds) DNA, peptide nucleic acid (PNA)−DNA complexes, and protein−DNA complexes, and potentially used as an all-electric sensor concept in gene profiling or fingerprinting for disease diagnostics and monitoring.[5−10]

The general operating principle is rather simple, as illustrated in Figure 1A and explained in detail elsewhere.[8] Briefly, in a nanopore device the pore channel is typically the largest source of electric resistance in the cell. When an ion current is driven through the system via an applied voltage, V_{bias}, any changes in the pore resistance thus result in a measurable change in the ion current, I, through the system. This occurs, for example, when DNA, charged particles, or proteins pass through the channel.[11−14] The ion-current modulation can be low (∼100 pA) and short-lived (<1 ms), depending on the analyte, the pore design, and the experimental conditions. In a simple case, one involving a cylindrical-pore channel, for example, the corresponding $I(t)$ modulation (translocation 'event' with a duration τ_e) is approximately rectangular in shape, but a substructure is usually found for more complex analytes. For example, a protein bound to DNA typically produces an individual spike (a 'subevent' with a duration τ_{se}) in the $I(t)$ trace that is superimposed on the actual DNA-translocation event.[15] Hence, the number and relative positions of the subevents can thus provide information on the number of bound proteins and potentially the thermodynamics of the binding equilibrium and the location of the proteins along the strand (if the translocation speed is known). Because the subevent duration is normally small compared with the event duration, $\tau_{se} \ll \tau_e$, resolving the subevents electrically can be challenging and

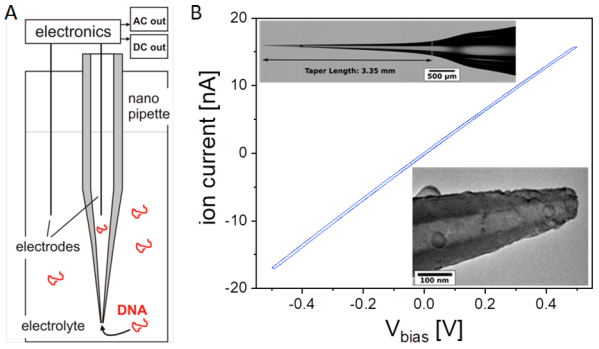

Figure 1. (A) Illustration of the experimental setup, cross-sectional view (not to scale). The quartz nanopipet is immersed in a liquid-filled cell, typically containing a highly concentrated chloride solution as the electrolyte. In our experiments, DNA was translocated from the outside to the inside of the pipet, as indicated. The custom-built detection electronics split the pore current into a slow (DC) and a fast (AC) channel, where the former contains the average pore current, and the latter contains the translocation events. (B) I/V_{bias} curve for a typical quartz nanopipet in 1 M KCl with 10 mM TE buffer. The conductance is G = 33.1 nS, as determined from the average of the slopes from the forward and reverse scan between ±0.1 V. The rectification ratio, RR, is 0.98 for these voltages. Top inset: optical micrograph showing the overall shape of the same pipet. Bottom inset: TEM image of the pipet's tip. The blob-like features are built up with imaging time and are most likely due to carbon contamination. The long taper length and conical shape, especially toward the pipet tip, are apparent.

requires the detection of rather low currents at high bandwidth. However, recent developments in instrument design now routinely allow for time resolutions well below 10 μs with nanopipets and even lower with nanopore chips.[16−19]

Meller and colleagues pioneered this concept with chip-based nanopores (diameter ∼5 nm, Si_3N_4 membrane) and two different types of PNA (specifically, bis-PNA and γ-PNA), to probe short base sequences in long pieces of dsDNA and ultimately genes.[6,7] PNA binds to dsDNA in a sequence-specific manner and with very high affinity, resulting in a local change in structure (bulging). The latter, in turn, produces a substructure in the translocation data, which can be related to the presence (or absence) of a particular gene sequence. Meller's group exploited this capability to differentiate subtypes of the HIV *pol-1* gene for pathogen classification.

A conceptually different approach is to employ artificial, engineered structures as carriers that have some function, such as protein-binding capability or a recognition element, engineered into them.[20,21] For example, Bell and Keyser used nanopipets and a carrier design based on DNA self-assembly to include first a sequence of structural features (dumbbells) as a 'barcode' identifying the DNA and second a site for antibody binding.[22] Different carriers may thus be identified in mixtures and several different proteins can be assayed at the same time (multiplexing), as the authors demonstrate with biotin, bromodeoxyuridine, puromycin, and digoxygenin modifications as antigens and their respective antibodies. Notably, similar engineered structures have also been used to characterize the translocation process itself, such as the translocation velocity and dynamics,[23,24] and for the detection of single-nucleotide polymorphisms.[25]

A similar idea, albeit based on aptamers, was pursued by Edel, Ivanov, and colleagues.[26] Specifically, the single-stranded (ss) ends of λ-DNA were modified with probes containing two parts: one complementary to the ss ends and a second one made of aptamer sequences optimized for thrombin and acetylcholinesterase binding. This yielded DNA constructs with protein-binding sites on either end, which were again analyzed by translocation through nanopipets (from the inside to the outside of the pipet in this case). The DNA carriers in earlier studies had to be fabricated by reconstituting the dsDNA from a long ss template and a large number of short, complementary strands, which was rather cumbersome and comparatively expensive. The approach of Edel and co-workers is somewhat simpler, as it starts with intact λ-DNA, albeit at the cost of reduced design flexibility and probe density. The authors also demonstrate translocation experiments in diluted human serum, which is a step toward the application of nanopore sensing in complex, perhaps more realistic media. That said, when coupled to suitable workflows, operation in such environments might not always be required.

Beamish, Tabard-Cossa, and Godin combine some of the above concepts in their recent work.[27] Using <5 nm pores in chip-based nanopore devices (SiN membrane, thickness ∼10 nm), prepared not by electron- or ion-beam drilling but by dielectric breakdown,[28] they employed DNA engineering to synthesize 255 base pair (bp) dsDNA scaffolds with ds overhangs as short as 15 bp. These overhangs could reliably be detected and resolved by ion-current sensing in a label-free manner. Moreover, the authors also prepared scaffolds with ssDNA overhangs that could bind an aptamer-based probe in the presence of ATP. The bound probe was then detected by nanopore sensing, as an indirect way of detecting ATP.

An interesting alternative approach for detecting hybridization of short DNA (and potentially other) targets is the use of modified nanoparticles. In particular, particles with magnetic cores can first be released into the sample medium, where they bind their targets, and then recaptured and preconcentrated using magnetic fields. Binding to the target then either changes the surface properties of the particles (e.g., ζ-potential), and hence their translocation characteristics (speed),[29,30] or produces altogether new structures (such as particle dimers),[31] which are then detected by resistive-pulse sensing. Although these approaches do not probe individual binding or hybridization sites, there appears to be some potential for multiplexed detection, for example, by employing particles of different sizes. Apart from simple target capture, such studies have also included site-specific detection of methylation sites.[32]

In our present work, we build on these advances and have developed a high-throughput sensing concept with new capabilities and applications, namely, with a focus on the label-free detection and quantification of short (∼100 nucleotides (nt)) ssDNA fragments. Such short ssDNA segments are found in blood, urine, and other bodily fluids as circulating cell-free DNA (cfDNA), where they have been implicated in disease diagnostics and monitoring, for example, in the context of urinary-tract infections.[33] In cancer, the ratio of short (<150 bp) versus long DNA in plasma is increased, most likely because of enhanced rates of cell apoptosis and necrosis.[34,35] Equally, such short DNA fragments may serve as diagnostic markers for infections, such as with *Mycobacterium tuberculosis* (TB)[36] or other pathogens. In the present proof-of-concept study, we show how resistive-pulse sensing in combination with suitable carrier design may be used to detect short DNA sequences in solution. Specifically, we designed 7.2 kbp dsDNA structures with either one or two

protrusions (overhangs) in specific locations along the carrier strand (see the Experimental Section and the Supporting Information, SI, for details). These protrusions comprised short (~12 bp) ds sections close to the carrier backbones and 88 nt ss sections that could be hybridized with their complementary sequences (the targets). In translocation experiments with quartz nanopipets, we then detected and differentiated ss and hybridized protrusions and hence determined the hybridization state of the overhang in a rapid and label-free manner.

RESULTS AND DISCUSSION

We chose identical sequences for the probe regions for all samples to allow for a comparison of different overhang locations. The sequence was taken from the *RV1910c* gene in TB, a gene-regulatory region of the KatG protein.[37] KatG is a catalase peroxidase that is responsible for activating isoniazid (INH), one of the most effective and specific antituberculosis drugs since its introduction in 1952.[38,39] Deregulation of the *KatG* gene thus triggers INH resistance in bacteria and renders the drug useless. Furthermore, INH resistance is often the first step toward multidrug resistance,[40] so robust and fast identification of antibiotic resistance could already inform the early stages of therapy. On the basis of our results, it appears that resistive-pulse sensing with nanopores and nanopipets could help address this need, in particular when coupled with a suitable workflow for sample extraction and amplification.

The quartz pipets used in this study were produced with a mechanical puller, and the exact geometry of the channel and the pore size at the pipet can vary to some degree. On the basis of conductance measurements and optical- and transmission-electron-microscopy (TEM) imaging, we found, however, that the device-to-device variation for the pulling parameters used was relatively small (see the Experimental Section). We typically obtained pipets with (inner) pore diameters at the tip between 20 and 30 nm, and we obtained good agreement between the different characterization methods. As an example, we show the current−voltage (I/V) characteristics (forward and reverse voltage sweeps), optical-microscopy image, and TEM image recorded for the same pipet in Figure 1B. From the average slope of the two sweeps between ±0.1 V, a conductance of 33.1 nS was obtained, which, in conjunction with eq S2 in the SI, was used to estimate a pore diameter of 29 nm. This compares well with the pore diameter determined by TEM, which yielded 31 nm for the same pipet. The TEM and optical images also revealed that the channel geometry was approximately conical over long distances, with an opening angle of about 15°. The small offset between the forward and reverse voltage scan was due to capacitive charging of the system, as discussed in detail elsewhere.[41,42]

The DNA structures under study here are illustrated in Figure 2A and comprise two pairs of samples, as mentioned above. Namely, these are two structures with a single overhang (ssx1 and hyx1) and two structures with two overhangs (ssx2 and hyx2); ssx refers to DNA carriers with single-stranded overhangs, and hyx refers to those in which the overhangs have been hybridized with an 88 nt complementary strand (as the model disease marker). On the basis of equilibrium binding considerations and taking into account the concentration conditions during the assembly, we found that the affinity of the complementary strand was high enough to ensure near quantitative binding for the hyx samples (see SI Section 1).

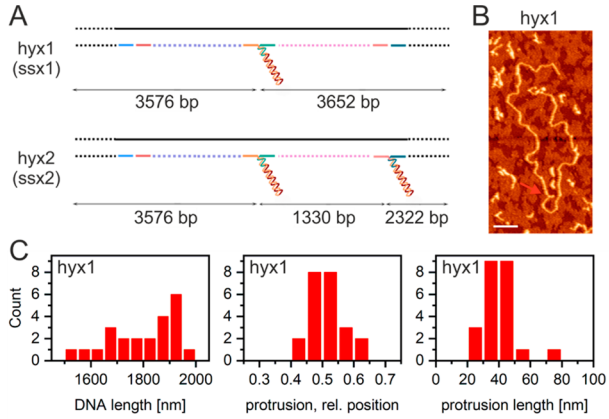

Figure 2. Design and initial characterization of the DNA structures under study. (A) Basic design of the samples with one or two overhangs (protrusions with suffixes 1 and 2, respectively) and the positions indicated: hyx, hybridized overhang; ssx, single-stranded overhang. The ss part of the overhang and its complementary target strand are ~88 nt long. (B) Typical AFM image of hyx1 in air (tapping mode) after drop-casting on mica (scale bar: 100 nm). The overhang is indicated with the red arrow. The short DNA fragments are impurities from the assembly process, as shown in the gel-chromatography data (SI Section 1) and the nanopore-translocation data, below. (C) Histograms of the DNA-carrier length and the relative position of the protrusion and its length (based on 23 DNA structures in total).

In order to confirm that the assembly had been successful, atomic-force-microscopy (AFM) characterization was performed in selected cases, as shown for hyx1 in Figure 2B). A small amount of shorter adsorbed fragments was also seen, which were still present in the sample solution. In this context, we felt that further purification was unnecessary, in light of the fact that in mixtures, the longer DNA carrier can readily be distinguished from shorter fragments in both AFM and nanopore sensing (see below). This is clearly a strength of the nanopore-sensor concept presented here, which can ultimately simplify workflows in real-life applications.

In terms of the structural analysis of the hyx1 species on the surface, we focused on a region-of-interest between 0.3 and 0.7 of the total DNA length and excluded features that had markedly different contrast than the DNA carrier itself (pointing to coiling, knotting, or random coadsorption of shorter DNA fragments). With regards to the DNA length, we found a rather broad distribution with an average of 1.85 ± 0.13 μm (cf. Figure 2C, left panel), which was somewhat shorter than the expected value of 2.46 μm (7228 bp as per design, 0.34 nm/bp). This has been observed by others before and is most likely due to the DNA on the surface not being fully stretched.[23] In support of this hypothesis, we found good agreement with the intended design for the relative position of the overhang (0.51 ± 0.05 vs expected, 0.51) and its length (39 ± 7 nm vs expected, 34 nm), as shown in the middle and right panels of Figure 2C. Hence, partial decomposition is not likely the reason for the shorter observed carrier length, unless it affects the carrier symmetrically on both sides.

Figure 3 shows the results of translocation experiments performed with the same hyx1 sample in three different nanopipets, each with (internal) pore diameters between 20 and 30 nm (V_{bias} = 0.7 V, 4 M LiCl and 10 mM TE electrolyte). In Figure 3A, all events (59 964) are combined in one (logarithmic) scatter density plot, $\log_{10}(\Delta I_e)$ versus

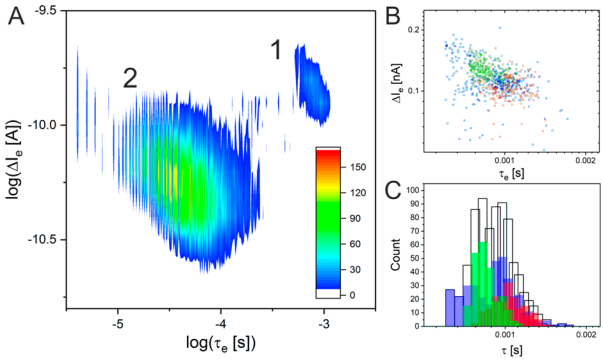

Figure 3. Translocation data from three different nanopipets for hyx1 (V_{bias} = 0.7 V, 4 M LiCl and 10 mM TE electrolyte). (A) Scatter density plot of $\log(\Delta I_e)$ vs $\log(\tau_e)$. Event clusters 1 and 2 emerge, where cluster 1 contains events from hyx1 (1166 out of a total of 59 964 events). These are of interest in the present context. Cluster 2 contains shorter DNA fragments that are still present in the sample, as discussed in the context of the AFM results above. (B) Scatter plot for cluster 1 only with the data points from the different pipets color-coded. Some small but systematic differences arise for the cluster centers. (C) One-dimensional τ_e histogram, showing the combined data set for cluster 1 (black, solid line) as well as the individual data for each pipet (same color-coding as in B). Comparison with translocation data from ssx1 (i.e., with the unhybridized overhang) reveals that the data are identical within experimental error (cf. Figure S7). This suggests that the hybridization state of the overhang does not significantly affect the translocation characteristics of the carrier DNA.

$\log_{10}(\tau_e)$. These events include electric noise and the translocation of short DNA fragments at short τ_e values, as well as the translocation of the DNA carriers at longer τ_e values. Two clusters, labeled 1 and 2, clearly emerge. Cluster 1 contains the translocation events from the longer DNA carriers (1166 events), in line with the translocation characteristics reported for similar DNA under comparable conditions.[16] Figure 3B,C shows a blow-up of cluster 1 and one-dimensional histograms, respectively, with the data color-coded according to the pipet used. The histogram in white with black solid line combines all three data sets. It is well-represented by a log-normal fit with a mean translocation time of $<\tau_e>$ = 0.94 ± 0.01 ms. However, as shown by the color-coded individual data sets, there are small but systematic differences among the individual nanopipets used. This is not surprising, because the channel dimensions are known to affect the translocation time and the associated current modulation.[43,8] Specifically, for larger pore diameters (d_p), τ_e and ΔI_e (relative to the mean pore current) decrease; for smaller d_p values, the opposite effect is observed. So, although every effort was made to use very similar nanopipets in the experiments, in terms of their conductance, G, the actual pore dimensions, and thus the translocation characteristics of an analyte, will not be exactly the same. The weighted average of the translocation times for all three pipets is $<\tau_e>$ = 1.0 ± 0.2 ms (weighted standard error) and hence the same as the previous value of the mean translocation time, within experimental error. The small relative shifts among the individual translocation-time distributions, however, lead to some broadening of the overall (combined) translocation-time distribution, which in turn affects the determination of related parameters, such as the effective diffusion coefficient of the DNA segment in the pore.[44] However, this aspect is not the focus of the present study, and we now turn to a discussion of the event substructure related to the presence of the different overhangs.

Three example events for each case (ssx1, hyx1, ssx2, and hyx2) are shown in Figure 4A, V_{bias} = 0.7 V), along with a graphical illustration of some parameters used for further analysis (cf. the Experimental Section). The ssx data are colored in green, and the hyx data are colored in red throughout Figure 4. Analogous data recorded at V_{bias} = 0.5 V using different pipets are shown in the SI. As expected, the samples featuring a single overhang approximately in the center of the construct (ssx1 and hyx1) displayed a subevent current spike approximately in the center of the respective event (see Section 3 of the SI for a discussion on DNA knotting). For the samples with two overhangs, ssx2 and hyx2, the situation is

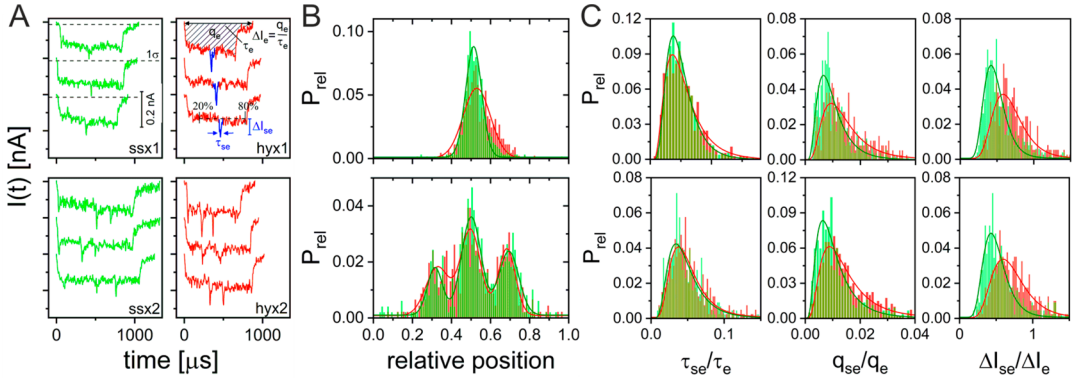

Figure 4. DNA-carrier-translocation data and analysis of subevents (V_{bias} = 0.7 V). (A) Three example events for each of the four DNA structures are shown: ssx1 (top left), hyx1 (top, right), ssx2 (bottom left), and hyx2 (bottom right). The color-coding for ssx (green) and hyx (red) is the same throughout this figure. Key parameters characterizing the events and subevents are illustrated, including the 1σ line defining event start and stop points according to our definition and the 20/80% boundary for the subevent search (see the Experimental Section). Some subevents, as defined by the search algorithm used here, are shown in blue. (B) Normalized histograms of the relative subevent positions for single-overhang samples (ssx1 and hyx1, top) and double-overhang samples (ssx2 and hyx2, bottom), including Gaussian fits. (C) Normalized histograms of subevent characteristics relative to the respective event: τ_{se}/τ_e, q_{se}/q_e, and $\Delta I_{se}/\Delta I_e$. All distributions are non-Gaussian and are represented well by log-normal fits (solid lines). Importantly, as the aim of the study is to distinguish hybridized (red) from nonhybridized overhangs (green), the difference between the two cases appears to be largest for the $\Delta I_{se}/\Delta I_e$ distributions. This is also the case for the data recorded at V_{bias} = 0.5 V (see SI).

more complex. Namely, the second, off-centered overhang can appear before or after the central one, depending on which part of the DNA carrier enters the pore first. This is illustrated in the examples given for ssx2 (bottom left), in which the off-centered overhang appears after the centered one in events 1 and 3 (top and bottom), and before the centered one in event 2 (middle). These considerations are also borne out in the statistical analysis of the subevent positions, as shown in Figure 4B for ssx1 and hyx1 (top) and ssx2 and hyx2 (bottom). Some further observations are worth noting: First, all events shown in Figure 4A share some common features in terms of their overall shape. Namely, they all start with a relatively sharp $I(t)$ transition as the DNA enters the pore channel from the outside, reflecting the relatively abrupt boundary between the pore entrance and the bulk solution. The current level then remains relatively constant until there is first an abrupt change and a nonlinear tail-off. Again, this most likely reflects the internal geometry of the pore channel and, in particular during tail-off, how the DNA leaves the narrowest part of the channel toward the bulk solution inside the pipet. With geometrically simple and well-defined analytes, such as spherical nanoparticles, this effect has previously been exploited to reconstruct the inner shape of the pore channel.[45] Second, the normalized histograms of the subevent positions for ssx1 versus hyx1 and for ssx2 versus hyx2 strongly overlap, suggesting that the hybridization state of the overhang has little effect on the translocation characteristics of the carrier DNA. This is despite the fact that the pore diameter is smaller than the lengths of the overhangs, which are in turn shorter than the persistence lengths of the double-stranded DNA (>35 nm).[46,47] The same conclusion is, however, also borne out in more detailed analysis of the translocation events, below. Finally, the peak positions for all four samples are in excellent agreement with expectations based on the DNA design and in accordance with the AFM data above. From Gaussian fitting, ssx1 and hyx1 feature a single peak at relative positions of 0.51 $\pm$ 0.04 and 0.53 $\pm$ 0.07 (normalized to τ_e, error of $\pm 1\sigma$). The value expected on the basis of the DNA design was 3576/7228 = 0.49 or (7228 − 3576)/7228 = 0.51, depending on the DNA orientation, a difference that is within experimental error. For comparison, the AFM characterization of hyx1 yielded a relative overhang position of 0.51 $\pm$ 0.05, vide supra. For ssx2, peaks occur at 0.32 $\pm$ 0.04, 0.50 $\pm$ 0.05, and 0.69 $\pm$ 0.05; those for hyx2 occur at 0.33 $\pm$ 0.06, 0.50 $\pm$ 0.05, and 0.68 $\pm$ 0.04 (the fit is the sum of three Gaussians). The expected values are 0.32 and 0.51 for the two overhangs in one translocation direction and 0.49 and 0.68 for the other. The combined peak positions are again in very good agreement with the experimental values, within error. We also note that the observed intensity ratio is approximately 1:2:1, which is expected if the two DNA ends enter the pore with roughly equal probability (actual values from triple Gaussian fits were 1:2.1:1.3 for ssx2 and 1:1.8:1.4 for hyx2). Taken together, these data strongly suggest that the preparation of the DNA designs was successful in all four cases.

We now address the key question of the present study, namely, whether the hybridization states of the overhangs can reliably be determined using resistive-pulse sensing under the present conditions. Three fundamental signal properties were explored in this context, namely, the subevent duration, τ_{se}; the subevent charge, q_{se}; and the maximum current within a subevent, ΔI_{se}. This was based on the consideration that a stiffer (hybridized) overhang may increase the residence time in the sensing zone (and hence τ_{se}), and that the increased presence of DNA could increase q_{se} or enhance blockage (thus ΔI_{se}). Because of the relatively large variance in each of these event characteristics, we found it necessary to normalize τ_{se}, q_{se}, and ΔI_{se} to the corresponding event properties for each event. Because the overhangs are either single-stranded or double-stranded in our DNA design, there is no obvious internal reference for this normalization process, in contrast to those of designs used by others.[22] Accordingly, the respective normalized histograms for all three cases, τ_{se}/τ_e, q_{se}/q_e, and $\Delta I_{se}/\Delta I_e$, are shown in Figure 4C (top: ssx1/hyx1, bottom: ssx2/hyx2, in green and red, respectively). The solid lines are fits to log-normal distributions, which generally provide a very good representation of the histograms. The individual values of the fit parameters are of less relevance here, but the fact that the data are not normally distributed affects the statistical analysis, as discussed below. From the histogram shapes it is apparent that of those three classification parameters, the $\Delta I_{se}/\Delta I_e$ histograms show the largest differences between the ssx and hyx samples. The same observations hold true for the data recorded with a different set of pipets at V_{bias} = 0.5 V, as shown in the SI (Section 5).

In order to test whether the observed differences in the $\Delta I_{se}/\Delta I_e$ distributions were statistically significant, we subsequently performed a three-factor analysis of variance (ANOVA) with two levels for each, taking into account the hybridization state of the overhangs (ssx vs hyx), the bias voltage (0.5 vs 0.7 V), and the number of overhangs per carrier (single vs double). In this context, it is worth reiterating that the overhangs in all samples have the same sequence composition. Accordingly, our analysis initially considers whether there is any significant difference between ssx and hyx, irrespective of the sample and conditions used. ANOVA is thus the preferred method, as it allows for multiple comparisons to be performed at the same time and provides information on the interactions between those factors. It is more conservative than performing multiple t tests and avoids an accumulation of type I errors (false positives).[48] In a second step, we also performed a series of post hoc Tukey−Kramer mean-difference tests for the individual comparisons (ssx1 vs hyx1 and ssx2 vs hyx2 at the two different voltages) to investigate the observed main effects and some of the interactions in more detail (cf. Sections 6 and 7 in the SI).

Focusing on the main effects here, the means of two factors, namely hybridization state and voltage, are significantly different at a 0.05 confidence level ($p \approx 0$ and 0.008, mean differences of −0.139 and 0.021, and sample sizes of 1266 (ssx), 1088 (hyx), 657 (0.5 V), and 1697 (0.7 V)), whereas the third factor, number of overhangs, is not significantly different (p = 0.061, mean difference of 0.015, sample sizes of 1224 (single overhang) and 1130 (double overhang)). The effect of hybridization state is clearly relevant to the underlying idea of the present work and will be explored in further detail below. A main effect of voltage could also be of interest in that it could suggest that optimization of V_{bias} could lead to improved sensor performance. However, as discussed in Section 7 of the SI, when considering interaction effects and suitable post hoc tests, the effect was found not to be statistically robust in terms of the individual comparisons (i.e., differentiation between ssx and hyx was similar at the two V_{bias} values studied). Finally, the absence of statistically significant effects for the number of overhangs would suggest that the latter does not affect the

detection of the individual subevents, at least in the present samples and conditions used.

To confirm whether the hybridized and nonhybridized overhangs in a given sample could indeed be differentiated in a statistically significant manner, we performed Tukey–Kramer mean-difference tests for each of the four relevant individual comparisons (cf. Figure S12A–D for ssx1 vs hyx1 and ssx2 vs hyx2 at V_{bias} = 0.5 and 0.7 V). Indeed, in all cases, the difference is found to be statistically significant at α = 0.05 (type I error rate). Moreover, the mean differences of the ssx and hyx samples have the same signs (−0.095, −0.199, −0.133, and −0.129, Figure S12A–D) and are on average of similar magnitude (i.e., there is no obvious difference between the single- and double-overhang samples, in accordance with the discussion above). Thus, the $\Delta I_{se}/\Delta I_e$ ratio is slightly but consistently larger for hybridized overhangs, compared with that for their single-stranded analogues.

Our results therefore confirm that the hybridization state of the overhangs may be detected in a statistically significant manner, on the basis of a sufficient number of translocation events. The comparison was based on 2354 samples, but a power analysis yielded a hypothetical power of 95% for a sample size of 100 (α = 0.05), an indication that a significantly smaller number of events may be sufficient to determine the hybridization state of the probes in a statistically significant manner. Nevertheless, the difference between ssx and hyx samples is relatively small at present, but it may be improved further. V_{bias} is a parameter we have considered in this context, but no significant dependence on V_{bias} was found.

Decreasing the pore size may be another strategy toward improving the sensor performance; it is known to improve the signal-to-noise ratio for translocation events.[43] Atomic-layer deposition (ALD) of oxides has been explored in this context and also in nanopipets.[49,50] However, care needs to be taken with regards to the identity and surface properties of the oxide as well as the preparation conditions. For example, we observed that some Al_2O_3 films were not stable under the experimental conditions used in the present study (i.e., at very high halide concentrations), in line with previous literature.[51−54] Moreover, in the presence of the Al_2O_3 layer, the channel surface is net positively charged,[49] leading to adsorption of the DNA to the pore surface, wider translocation-time distributions, and fewer well-resolved individual events. Hence, a different oxide, for example, SiO_2, with a negative surface charge in solution may be preferable in this regard.

In conclusion, we have demonstrated how nanopipet-based electric detection combined with robust statistical analysis is capable of probing the hybridization state of short, approximately 100 nt long single-stranded overhangs. Their lengths are comparable to those of short circulating DNA fragments, which are found in different bodily fluids and have been identified as potential markers in disease diagnostics, for example, in TB detection. To illustrate this aspect, the 88 nt probe design employed in this study was taken from the *RV1910c* gene, a gene-regulatory region known to play a key role in TB resistance against INH. With the overhangs arranged over a long DNA carrier, the sensing strategy also encompasses some multiplexing capabilities. Not only is it possible to integrate a larger number of probes in one carrier (of equal or different sequence composition), but also to mix carriers of different lengths (and different overhangs). Equally, it would also be possible to encode specific features into the carriers (such as hairpins), to differentiate those of equal length.[22] Notably, while the carrier designs used in the present study have been implemented using DNA self-assembly from small fragments, similar structures may be created involving enzymatic modification of dsDNA.[55−58] The latter may be significantly more cost-effective and enable the preparation of larger amounts, both required for a viable sensor technology in the future. Following first efforts to improve the sensor performance, we have identified a small number of parameters to be explored in this context in the future. Finally, our study demonstrates the remarkable sensitivity of electric, nanopipet-based sensing toward the detection of even minor changes in DNA structure or composition in a label-free manner.

EXPERIMENTAL SECTION

Preparation and Characterization of the DNA Constructs. The synthesis was adapted from Bell et al. and Plesa et al.[22,23] The restriction enzymes (RE, *Bam*HI-HF and *Eco*RI-RF), M13mp18 circular ssDNA, and M13mp18 RF circular dsDNA were purchased from New England Biolabs (NEB). The 190 staples, ssDNA-overhang sequences, and target-DNA sequence were purchased from Integrated DNA Technologies (IDT). The sequences for the staples were similar to the ones reported by Bell et al.[19] These overhang and target-strand sequences can be found in the SI.

The M13mp18 ssDNA was linearized to form the DNA-carrier strand. Oligonucleotides with the sequence 5′-TCT AGA GGA TCC CCG GGT ACC GAG CTC GAA TTC GTA ATC-3′ were hybridized to the ssDNA to form a double-stranded restriction site recognizable by the RE. For the hybridization and RE cutting, 5 μL of M13mp18 (250 ng/μL), 5 μL of 10× NEB Cut Smart Buffer, 1 μL of oligonucleotide (100 μM), and 37 μL of autoclaved ultrapure water were mixed. To hybridize the oligonucleotide, the mixture was heated to 65 °C for 5 min, cooled at 25 °C for 5 min, and then cooled further at 10 °C for 10 min in a thermocycler (Eppendorf Mastercycler Gradient).

Afterward, 1 μL of *Bam*HI-HF and 1 μL of *Eco*RI-HF (20 000 U/mL) were added to the mixture. The mixture was incubated in the thermocycler at 37 °C for 2.5 h and then heated to 65 °C for 20 min to denature the RE. The ssDNA was cleaned up using the Monarch PCR and DNA Clean-Up kit (NEB) and eluted in autoclaved TE buffer (10 mM Tris-HCl and 1 mM EDTA, pH 7.8; Sigma-Aldrich). A purity check (running the eluted DNA on an 0.8% agarose gel) was performed after each digestion. The final concentration of the ssDNA was measured with UV–vis spectroscopy (Nanodrop 1000, Thermo Scientific). The same procedure (without hybridization) was also used to form the linearized dsM13mp18 from circular M13mp18-RF.

To form the dsDNA-carrier strand with one double-stranded overhang, 42 μL of linearized M13mp18 (11 nM), 1 μL of staple mix (38 bp oligonucleotides, each at 30 μM), 2 μL of both overhang strands (short and long, 100 μM each), 2 μL of target sequence (100 μM), 5 μL of $MgCl_2$ (100 mM), and 8 μL of autoclaved ultrapure water were mixed. The mixture was heated to 72 °C and cooled at a rate of 1 °C every 4 min until the temperature dropped to 23 °C. The excess staples, overhangs, and target strands were (partially) removed using Amicon Ultra 100 kDa cutoff centrifugal filters (Millipore). The purification step consisted of diluting the mixture with 400 μL of TE buffer and then centrifuging at 3000*g* for 10 min at 4 °C. The filtrate was then decanted and the above procedure

was repeated for six washing steps. The sample was recovered by inverting the filter and centrifuging at 1000*g* for 2 min. The product quality and quantity were initially characterized by gel electrophoresis and UV−vis spectroscopy. A similar procedure was carried out to form constructs with a single (unhybridized) ss-overhang and those with two overhangs.

AFM Studies. The DNA samples were imaged in tapping mode in air at 23 °C with an Agilent 5500 AFM/SPM microscope (Keysight Technologies) and commercial PointProbe Plus-NCHR-10 probes (Windsor Scientific). Images were processed with plane and flatten filters in the WSxM 5.0 Develop 7.0 software.[59] To prepare the substrate, the buffer (10 mM HEPES, pH 7.6; 4 mM $MgCl_2$; 1 mM EDTA; Sigma-Aldrich) was filtered using a 0.2 μm syringe filter (EMD Millipore) to remove any large particle contaminants and then autoclaved. The construct (1.5 ng/μL) was prepared in 20 μL of the said buffer and deposited on freshly cleaved Mica (9.9 mm diameter, Agar Scientific). The DNA was left to adsorb to the surface for 5−10 min. The surface was then rinsed with 1 mL of nuclease-free water (NEB) three times and dried in a N_2-gas flow.

Nanopipet Fabrication and Characterization. Nanopipets were made from filamented quartz capillaries (1 mm o.d., 0.5 mm i.d., 7.5 cm length; Sutter Instruments). The capillaries contained a ∼160 μm glass filament that facilitated the filling of the nanopipet with electrolyte by capillary action.[60] The glass capillaries were first plasma-cleaned for 7 min (Harrick Scientific) before being loaded into the laser pipet puller (P2000, Sutter Instruments). The pulling program involved two steps and the following parameter settings: step 1 (heat: 880−890, filament: 4, velocity: 30, delay: 175−190, pull: 100−110) and step 2 (heat: 900, filament: 1, velocity: 15−20, delay: 170−175, pull: 160). Minor reoptimization of the parameter settings was sometimes required, when the apparent pore diameters consistently veered off the desired range from 20 to 30 nm (as judged by the pore conductance, vide infra). This was most likely due to small changes in the environmental conditions (humidity or ambient temperature) or in the puller itself, but those changes were small, as shown above. The inner diameter of the nanopore at the end of the pipet was initially estimated from the conductance of the pipet (see SI) in 1 M KCl and, in some cases, characterized further using TEM. For translocation experiments, the pipets were then integrated into a custom-built liquid cell with one Ag/AgCl electrode on the inside and the other one on the outside of the pipet.

TEM Characterization of the Pipets. TEM imaging of the nanopipets was carried out using a JEOL JEM-2100F TEM. The measurement of the images was conducted using ImageJ.[61] Sample preparation involved the following: The tip of the pipet was positioned such that it was sitting parallel to the center of the Cu TEM slot grid (catalogue no. GG030, Taab Laboratory Equipment Ltd.) and glued to the grid with a two-component epoxy glue (Araldite). The glue was left to set for 6 h, after which the pipet attached to the grid was cleaned under UV and ozone for 20 min (UVOCS). It was then sputter coated (Polaron Quorum Technologies) with 10 nm Cr to reduce charging effects. The parts of the pipet lying just outside the grid were cut off using a scalpel before the grid was placed in the sample holder of the TEM.

Translocation Experiments. Translocation experiments were performed in 4 M LiCl electrolyte, which is known to reduce the translocation speed in comparison with that of KCl,[62,63] using a custom-made, low-noise, wide-bandwidth current amplifier reported previously.[16,17] The electronics output is split into DC and AC channels, containing slow (below 10 Hz) and fast (>10 Hz) modulations of the current, respectively. Specifically, this means that translocation events appear in the AC output. It is zero mean, which greatly simplifies any background correction (minor constant offsets were corrected prior to the event search, vide infra). The DC channel contains the steady-state current through the cell, which is related to the pore conductance. The AC output is filtered as specified with an eight-pole low-pass (analogue) Bessel filter (Krohn-Hite Corporation). A digital oscilloscope (Picoscope 4262, Pico Technology) served as an analogue-to-digital converter at a 1 μs sampling rate. Custom-written Matlab code was used for instrument control and data acquisition and analysis, as detailed below. The liquid cell and the amplifier were housed in a double Faraday cage to minimize electrical noise. In total, 23 different nanopipets were used in the translocation experiments presented in this work.

Analysis of the Translocation Data. Current−time traces were initially subjected to a zero-order background correction to account for minor, constant offsets in the AC-channel output (typically <10 pA). Then, a threshold search was performed with a 5σ cutoff, where σ is the standard deviation of the current noise in the AC channel. The search algorithm then found the data points, which first crossed the zero baseline, relative to the 5σ cutoff, as well as the corresponding 1σ values. The latter served as definition for the event start and stop, as a compromise between minimizing the effect of local baseline fluctuation on the event characteristics and our ambition to capture the overall event shape as much as possible. Thus, the 1σ event duration is $\tau_e = t_{stop} - t_{start}$. The probability distribution of τ_e was found to be skewed and well-approximated heuristically by a log-normal distribution.[16,17] For a physically rigorous closed-form solution of the distribution function, see ref 44. The effective event magnitude, ΔI_e, was calculated from the integral of the $I(t)$ trace between t_{start} and t_{stop}, q_e, divided by τ_e.

Subevents are more challenging to identify and analyze, because they typically contain far fewer data points than the events themselves. We therefore took a somewhat different approach in searching for and analyzing those subevents. First, the median of a central section of the event (0.2 to 0.8 relative event duration) was determined to serve as baseline (the median, rather than the mean, was chosen to be less sensitive to outliers, such as spikes). Subevents were identified in a threshold search with a 1.2 × ΔI_e cutoff. The search algorithm also extracted all adjacent data points before and after, until the median value was reached. The subevent duration, τ_{se}, was thus the time difference between the first median crossing after the subevent threshold was reached and the last median crossing before the threshold value (capturing a large part of the subevent shape). ΔI_{se} was taken to be the maximum current, relative to the median, and q_{se} was determined from the integral of the $I(t)$ trace within a subevent. In absence of a closed-form solution for the distribution functions of $\Delta I_{se}/\Delta I_e$, q_{se}/q_e, and τ_{se}/τ_e, the corresponding probability distributions were also approximated by log-normal distributions. These were mainly used for illustration purposes and to highlight the non-normality of the data in the context of the subsequent statistical analysis.

ASSOCIATED CONTENT

Supporting Information

The Supporting Information is available free of charge on the ACS Publications website at DOI: 10.1021/acs.analchem.8b04357.

DNA-carrier design and characterization; modeling results of the field distribution in the nanopipet and of the binding equilibrium between the DNA-capture probe and the carrier; additional nanopore translocation data at V_{bias} = 0.5 V; and further discussion of the statistical tests, including three-way ANOVA (PDF)

AUTHOR INFORMATION

Corresponding Author

*E-mail: t.albrecht@bham.ac.uk.

ORCID

M. A. McLachlan: 0000-0003-3136-1661

A. E. G. Cass: 0000-0001-8881-4786

T. Albrecht: 0000-0001-6085-3206

Author Contributions

T.A. conceived the experiment. T.A., A.Y.Y.L., and C.H.B. performed the experiments and analyzed the data. The manuscript was written with contributions from all authors.

Notes

The authors declare no competing financial interest.

ACKNOWLEDGMENTS

The authors thank Willem van Schaik (Institute for Global Innovation and Institute of Microbiology and Infection, University of Birmingham, U.K.), Robert Neely (School of Chemistry, University of Birmingham, U.K.), and Katja Kornysheva (Department of Psychology, Bangor University, U.K.) for discussions. The datasets generated or analyzed for the current study and the analysis scripts are available from the corresponding author upon reasonable request.

REFERENCES

(1) Luo, L.; German, S. R.; Lan, W.-J.; Holden, D. A.; Mega, T. L.; White, H. S. *Annu. Rev. Anal. Chem.* **2014**, *7*, 513−535.

(2) Wanunu, M. *Phys. Life Rev.* **2012**, *9*, 125−158.

(3) Steinbock, L. J.; Otto, O.; Chimerel, C.; Gornall, J.; Keyser, U. F. *Nano Lett.* **2010**, *10*, 2493−2497.

(4) Steinbock, L. J.; Lucas, A.; Otto, O.; Keyser, U. F. *Electrophoresis* **2012**, *33*, 3480−3487.

(5) Wanunu, M.; Sutin, J.; Meller, A. *Nano Lett.* **2009**, *9*, 3498−3502.

(6) Singer, A.; Wanunu, M.; Morrison, W.; Kuhn, H.; Frank-Kamenetskii, M.; Meller, A. *Nano Lett.* **2010**, *10*, 738−742.

(7) Singer, A.; Rapireddy, S.; Ly, D. H.; Meller, A. *Nano Lett.* **2012**, *12*, 1722−1728.

(8) Albrecht, T. *Curr. Op. Electrochem.* **2017**, *4*, 159−165.

(9) Stoloff, D. H.; Wanunu, M. *Curr. Opin. Biotechnol.* **2013**, *24*, 699−704.

(10) Miles, B. N.; Ivanov, A. P.; Wilson, K. A.; Dogan, F.; Japrung, D.; Edel, J. B. *Chem. Soc. Rev.* **2013**, *42*, 15−28.

(11) Bezrukov, S. M.; Vodyanoy, I.; Parsegian, V. A. *Nature* **1994**, *370*, 279−281.

(12) Li, J.; Gershow, M.; Stein, D.; Brandin, E.; Golovchenko, J. A. *Nat. Mater.* **2003**, *2*, 611−615.

(13) Plesa, C.; Kowalczyk, S. W.; Zinsmeester, R.; Grosberg, A. Y.; Rabin, Y.; Dekker, C. *Nano Lett.* **2013**, *13*, 658−663.

(14) Firnkes, M.; Pedone, D.; Knezevic, J.; Doblinger, M.; Rant, U. *Nano Lett.* **2010**, *10*, 2162−2167.

(15) Kowalczyk, S. W.; Hall, A. R.; Dekker, C. *Nano Lett.* **2010**, *10*, 324−328.

(16) Fraccari, R. L.; Ciccarella, P.; Bahrami, A.; Carminati, M.; Ferrari, G.; Albrecht, T. *Nanoscale* **2016**, *8*, 7604−7611.

(17) Fraccari, R. L.; Carminati, M.; Piantanida, G.; Leontidou, T.; Ferrari, G.; Albrecht, T. *Faraday Discuss.* **2016**, *193*, 459−470.

(18) Nuttall, P.; Lee, K.; Ciccarella, P.; Carminati, M.; Ferrari, G.; Kim, K.-B.; Albrecht, T. *J. Phys. Chem. B* **2016**, *120*, 2106−2114.

(19) Rosenstein, J. K.; Wanunu, M.; Merchant, C. A.; Drndic, M.; Shepard, K. L. *Nat. Methods* **2012**, *9*, 487−492.

(20) Bell, N. A. W.; Keyser, U. F. *J. Am. Chem. Soc.* **2015**, *137*, 2035−2041.

(21) Kong, J.; Bell, N. A. W.; Keyser, U. F. *Nano Lett.* **2016**, *16*, 3557−3562.

(22) Bell, N. A. W.; Keyser, U. F. *Nat. Nanotechnol.* **2016**, *11*, 645−652.

(23) Plesa, C.; van Loo, N.; Ketterer, P.; Dietz, H.; Dekker, C. *Nano Lett.* **2015**, *15*, 732−737.

(24) Bell, N. A. W.; Chen, K.; Ghosal, S.; Ricci, M.; Keyser, U. F. *Nat. Commun.* **2017**, *8*, 380.

(25) Kong, J.; Zhu, J.; Keyser, U. F. *Chem. Commun.* **2017**, *53*, 436−439.

(26) Sze, J. Y. Y.; Ivanov, A. P.; Cass, A. E. G.; Edel, J. B. *Nat. Commun.* **2017**, *8*, 1552.

(27) Beamish, E.; Tabard-Cossa, V.; Godin, M. *ACS Sensors* **2017**, *2*, 1814−1820.

(28) Kwok, H.; Briggs, K.; Tabard-Cossa, V. *PLoS One* **2014**, *9*, No. e92880.

(29) Blundell, E. L. C. J.; Vogel, R.; Platt, M. *Langmuir* **2016**, *32*, 1082−1090.

(30) Vogel, R.; Pal, A. K.; Jambhrunkar, S.; Patel, P.; Thakur, S. S.; Reátegui, E.; Parekh, H. S.; Saá, P.; Stassinopoulos, A.; Broom, M. F. *Sci. Rep.* **2017**, *7*, 17479.

(31) Ang, Y. S.; Yung, L.-Y. L. *ACS Nano* **2012**, *6*, 8815−8823.

(32) Healey, M. J.; Rowe, W.; Siati, S.; Sivakumaran, M.; Platt, M. *ACS Sens* **2018**, *3*, 655−660.

(33) Burnham, P.; Dadhania, D.; Heyang, M.; Chen, F.; Westblade, L. F.; Suthanthiran, M.; Lee, J. R.; De Vlaminck, I. *Nat. Commun.* **2018**, *9*, 2412.

(34) Jiang, P.; Lo, Y. M. D. *Trends Genet.* **2016**, *32*, 360−371.

(35) Gravina, S.; Sedivy, J. M.; Vijg, J. *Aging Cell* **2016**, *15*, 398−399.

(36) Yamamoto, M.; Ushio, R.; Watanabe, H.; Tachibana, T.; Tanaka, M.; Yokose, T.; Tsukiji, J.; Nakajima, H.; Kaneko, T. *Int. J. Infect. Dis.* **2018**, *66*, 80−82.

(37) Siu, G. K. H.; Yam, W. C.; Zhang, Y.; Kao, R. Y. T. *Antimicrob. Agents Chemother.* **2014**, *58*, 6093−6100.

(38) Ando, H.; Kitao, T.; Miyoshi-Akiyama, T.; Kato, S.; Mori, T.; Kirikae, T. *Mol. Microbiol.* **2011**, *79*, 1615−1628.

(39) Bernstein, J.; Lott, W. A.; Steinberg, B. A.; Yale, H. L. *Am. Rev. Tuberc.* **1952**, *65*, 357−364.

(40) Caminero, J. A. *Int. J. Tuberc. Lung Dis.* **2010**, *14*, 382−390.

(41) Albrecht, T. *ACS Nano* **2011**, *5*, 6714−6725.

(42) Rutkowska, A.; Edel, J. B.; Albrecht, T. *ACS Nano* **2013**, *7*, 547−555.

(43) Wanunu, M.; Sutin, J.; McNally, B.; Chow, A.; Meller, A. *Biophys. J.* **2008**, *95*, 4716−4725.

(44) Ling, D. Y.; Ling, X. S. *J. Phys.: Condens. Matter* **2013**, *25*, 375102.

(45) Lan, W.-J.; Holden, D. A.; Zhang, B.; White, H. S. *Anal. Chem.* **2011**, *83*, 3840−3847.

(46) Hagerman, P. J. *Annu. Rev. Biophys. Biophys. Chem.* **1988**, *17*, 265−286.

(47) Brinkers, S.; Dietrich, H. R. C.; de Groote, F. H.; Young, I. T.; Rieger, B. *J. Chem. Phys.* **2009**, *130*, 215105.

(48) Howell, D. *Statistical Methods for Psychology*, international ed.; Wadsworth Publishing, 2012.

(49) Chen, P.; Mitsui, T.; Farmer, D. B.; Golovchenko, J.; Gordon, R. G.; Branton, D. *Nano Lett.* **2004**, *4*, 1333−1337.

(50) Venkatesan, B. M.; Dorvel, B.; Yemenicioglu, S.; Watkins, N.; Petrov, I.; Bashir, R. *Adv. Mater.* **2009**, *21*, 2771−2776.
(51) Potts, S. E.; Schmalz, L.; Fenker, M.; Díaz, B.; Świątowska, J.; Maurice, V.; Seyeux, A.; Marcus, P.; Radnóczi, G.; Tóth, L.; Kessels, W. M. M. *J. Electrochem. Soc.* **2011**, *158*, C132−C138.
(52) Liu, M.; Jin, Y.; Zhang, C.; Leygraf, C.; Wen, L. *Appl. Surf. Sci.* **2015**, *357*, 2028−2038.
(53) Natishan, P. M.; O'Grady, W. E. *J. Electrochem. Soc.* **2014**, *161*, C421−C432.
(54) Díaz, B.; Härkönen, E.; Maurice, V.; Światowska, J.; Seyeux, A.; Ritala, M.; Marcus, P. *Electrochim. Acta* **2011**, *56*, 9609−9618.
(55) Deen, J.; Wang, S.; Van Snick, S.; Leen, V.; Janssen, K.; Hofkens, J.; Neely, R. K. *Nucleic Acids Res.* **2018**, *46*, e64.
(56) Lauer, M. H.; Vranken, C.; Deen, J.; Frederickx, W.; Vanderlinden, W.; Wand, N.; Leen, V.; Gehlen, M. H.; Hofkens, J.; Neely, R. K. *Chem. Sci.* **2017**, *8*, 3804−3811.
(57) Deen, J.; Vranken, C.; Leen, V.; Neely, R. K.; Janssen, K. P. F.; Hofkens, J. *Angew. Chem., Int. Ed.* **2017**, *56*, 5182−5200.
(58) Chen, K.; Juhasz, M.; Gularek, F.; Weinhold, E.; Tian, Y.; Keyser, U. F.; Bell, N. A. W. *Nano Lett.* **2017**, *17*, 5199−5205.
(59) Horcas, I.; Fernández, R.; Gómez-Rodríguez, J. M.; Colchero, J.; Gómez-Herrero, J.; Baro, A. M. *Rev. Sci. Instrum.* **2007**, *78*, 013705.
(60) *P-2000 Laser-Based Micropipette Puller System Operation Manual*; Sutter Instruments, 2012.
(61) Schneider, C. A.; Rasband, W. S.; Eliceiri, K. W. *Nat. Methods* **2012**, *9*, 671−675.
(62) Uplinger, J.; Thomas, B.; Rollings, R.; Fologea, D.; McNabb, D.; Li, J. *Electrophoresis* **2012**, *33*, 3448−3457.
(63) Kowalczyk, S. W.; Wells, D. B.; Aksimentiev, A.; Dekker, C. *Nano Lett.* **2012**, *12*, 1038−1044.